Mesoporous TiO_2 Support Materials for Ru-Based CO_2 Methanation Catalysts

Ara Kim,[a,b] Clément Sanchez,[b] Bernard Haye,[b] Cédric Boissière,[b] Capucine Sassoye,[b] Damien P. Debecker[a]**

[a] Institute of Condensed Matter and Nanosciences (IMCN), UCLouvain, Place Louis Pasteur, 1, box L4.01.09, 1348 Louvain-La-Neuve, Belgium. E-mail: damien.debecker@uclouvain.be

[b] Sorbonne Universités, UPMC Université Paris, CNRS, Collège de France, Laboratoire de Chimie de la Matière Condensée de Paris, 4 Place Jussieu, 75252 Paris Cedex, France. E-mail: capucine.sassoye@upmc.fr

Keywords: Mesoporous TiO_2, aerosol, spray drying, CO_2 hydrogenation, RuO_2 nanoparticles, methanation

Abstract: Mesoporous TiO_2 materials have been prepared by an aerosol process, which leverages on the acetic acid-mediated sol-gel chemistry and on the evaporation-induced self-assembly of surfactants to obtain materials with high specific surface area and large mesoporous volume. The obtained spherical particles are calcined to release the porosity. It is shown that the mesoscopic order can be preserved when the calcination is carried out at relatively low temperature (375 °C and below). Harsher calcination conditions provoke the progressive destruction of the mesostructure, concomitant with a progressive drop of textural properties and with the crystallization of larger anatase domains. The mesoporous TiO_2 material calcined at 350°C (specific surface area = 260 $m^2.g^{-1}$; pore volume = 0.36 $cm^3.g^{-1}$; mean pore diameter = 5.4 nm) was selected as a promising support for preformed RuO_2 nanoparticles. It is shown that the impregnation of RuO_2 nanoparticles and subsequent annealing provoke intense modifications of the texture and crystallinity of the TiO_2 materials. In addition to a drop in the textural parameters, a RuO_2-mediated crystallization of rutile TiO_2 is highlighted at a temperature as low as 250°C. After an in situ reduction in H_2, the catalysts containing TiO_2 rutile and maintaining relatively small RuO_2 crystals showed the highest activity in the methanation of CO_2 (up to 2.05 $\mu mol_{CH4}.g_{cat}^{-1}.s^{-1}$) .

1. Introduction

Considering the impact of human activities on the atmospheric CO_2 levels and the related effects on climate change, the need to curve our net CO_2 emissions is pressing.[1] The catalytic hydrogenation of CO_2 towards methane, also called the Sabatier reaction or CO_2 methanation, is currently being intensely investigated as a suitable way to activate CO_2, turning a waste into a fuel at the cost of H_2 (which must be produced using renewable energy).[2-6] CO_2 methanation is seen as a key enabling technology for the storage of surplus electricity from fluctuating renewable sources.[7-8] Heterogeneous catalysts based on Ni, Ru, Pd, Co, Rh, Fe, etc.[9-15] show CO_2 methanation activity, but Ru is known to be the most active at mild temperature.[3, 16-17] For such reactions, the nature of the support is crucial, and TiO_2 materials have been identified as best supports for Ru.[4]

Catalysts preparation methods that allow the deposition of highly dispersed Ru on a TiO_2 support tend to lead to higher activity (e.g. the barrel-sputtering method proposed by Abe et al.[18]). Recently, Behm et al. highlighted the decisive role of the specific surface area of the TiO_2 support on the dispersion of Ru, showing a beneficial effect of using a support with high SSA (as compared to the most common low-SSA supports).[19] Moreover, it was shown that the crystalline structure of the titania support plays a decisive role in the formation of a highly active Ru/TiO_2 CO_2 methanation catalyst, and this was explained by studying the active phase-support interaction in the RuO_2-TiO_2 system during calcination.[20-22] On the one hand, RuO_2 does not disperse on anatase TiO_2 and segregates in the form of large chunks with low activity. On the other hand, RuO_2 forms a dispersed epitaxial layer on rutile TiO_2 favoring a high Ru dispersion and high activity.[23] Thus, the nature of the active phase-support interactions, governed by the TiO_2 support crystallinity, dictates the catalytic activity of the metallic Ru-species obtained after in situ reduction. The highest catalytic activity was obtained when a non-sintering rutile TiO_2 is used as a support.[20, 22] Such

materials, however typically have low specific surface area, which limits the amount of Ru that can dispersed. This prompted us to explore mesoporous and amorphous TiO_2 materials with high surface area as a support for Ru-based methanation catalysts.

Sol-gel chemistry is recognized as a powerful toolbox for the preparation of such solids, often allowing to respond to strict specifications in terms of texture, composition, homogeneity, surface chemistry, etc.[24-27] Yet, the design and synthesis of mesoporous transition metal oxides is not as extensively studied as silica-based mesostructured materials[28] for their synthesis is more difficult to control. This is attributed to the different sol-gel condensation kinetics of silicate and non-silicate precursors.[29] Many metal oxide precursors are highly reactive toward water due to coordination expansion and rapid condensation.[30] As a consequence, several strategies are developed for the stabilization of inorganic precursors in solution including the use of reactivity-modifiers (i.e. complexing agents)[30-32] or the use of non-hydrolytic conditions.[33-35] A successful strategy based on the use of acetic acid has been demonstrated by Doeuff et al.[32] and Fan et al.[30] In the starting alkoxide solution containing acetic acid, hydrochloric acid, and ethanol, the strong acid (HCl) serves as a catalyst for the esterification of acetic acid with ethanol to produce water. It was demonstrated that the acetate ligands are directly bonded to the metal cores of metal alkoxide in a bidentate and bridging fashion to form stable, nanometer-sized metal oxo-acetate particles,[36] which slows down the hydrolysis process, thereby increasing the time of gelation.

The aerosol-assisted sol-gel process (AASG) integrates (i) sol-gel chemistry, (ii) aerosol spray handling and (iii) evaporation-induced self-assembly.[37] It has been proposed as a simple, continuous and rapid mode of production of high surface area-nanostructured materials with well-defined pore size and controllable texture.[37-39] This has proven highly effective for the preparation of a wide range of oxide and mixed oxide catalysts.[40-48] In this process, a stable solution of

precursors and surfactants is atomized into droplets (aerosol) and processed by contact with a drying gas. Upon solvent evaporation, surfactant molecules form micelles and reactive precursors undergo polycondensation reactions to form a solid inorganic network. Porosity is then released through a thermal treatment step designed as to remove the organic template.

In the present study, we synthesize mesoporous TiO_2 with high surface area, using the coupling of acetic acid mediated sol-gel chemistry with aerosol-assisted self-assembly process (Figure 1). The effect of calcination on the properties of the obtained mesostructured TiO_2 was studied by characterizing the solid with a series of techniques. One of the resulting mesoporous TiO_2 with preserved mesostructured was used as a support for preformed RuO_2 nanoparticles[49] and then calcined and reduced to be tested in the catalytic CO_2 methanation.

2. Experimental

2.1. Preparation of mesoporous TiO_2 by the aerosol-assisted sol-gel process

The synthesis of mesoporous TiO_2 via aerosol-assisted self-assembly process is described schematically in Figure 1. The procedure was adapted from Stucky et al.[36] The setup for the aerosol-assisted self-assembly process is illustrated in Figure 1 (supplementary information). An aerosol generator from TSI (model 9306) was employed; a pump was used to carry the aerosol towards the collection of dried powder. The precursor solution was prepared by dissolving Titanium (IV) butoxide precursor, acetic acid, and hydrochloric acid (37 wt.%) in ethanol. The molar ratio of the components was $Ti(OBu)_4$: acetic acid : HCl : EtOH : F127 = 1 : 4 : 1.2 : 40 : 0.01 (water from concentrated HCl gives a metal to water ratio of 1 to 4). To form nanometer-sized stable metal oxo-acetate precursor particles, the amphiphilic block copolymer F127 ($EO_{106}PO_{70}EO_{106}$, 12000 $g.mol^{-1}$) was added after stirring for 2 h. The solution was stirred vigorously for at least one more hour to obtain a clear solution and transferred to a closed container

attached to the aerosol generator. During the aerosol spray process, the surfactant-directed assembly gradually occurred during droplet drying across the heating zone (1 m-long quartz tube with a diameter of 8 cm, placed in a tubular oven set at 400°C). The dried powder was collected on a membrane filter with pore size of 0.2 µm. The gas flow was kept constant within the drying zone throughout the process with an oil bubbler, which also gave an indication of the pressure drop increase as the cake builds up on the filter during the process. The collected powder was carefully spread out in a shallow crucible(s) as a thin layer and calcined at various calcination temperatures (325, 350, 375, 400, 425, or 450 °C) for 5 h with 1 °C/min heating rate in static air to remove the surfactant and release the mesoporosity. The obtained titania materials are denoted as "TiX", where X represents the calcination temperature, in °C (Table 1).

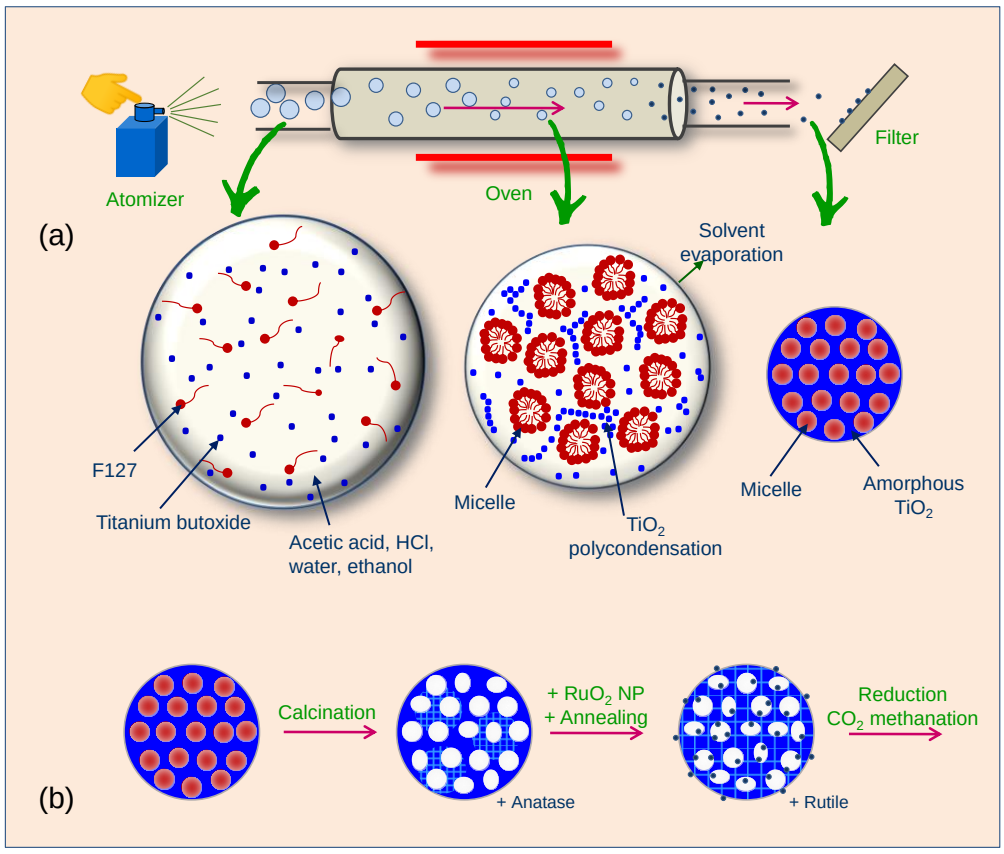


Figure 1. Schematic view of the materials preparation via the aerosol process.[37] (a) The precursor solution is atomized using compressed air. The aerosol mist is carried through a tubular furnace where solvent evaporation, surfactant self-assembly, and TiO_2 polycondensation occur. The dried particles – consisting of amorphous TiO_2 and surfactant micelles – are collected on an absolute filter. (b) The aerosol-produced particles are calcined in air to release the porosity (this also triggers partial pore collapse and initiates TiO_2 crystallization). RuO_2 nanoparticles are impregnated onto the mesoporous supports and annealed in air (this triggers further TiO_2 crystallization, also in the form of TiO_2 rutile). The resulting particles are tested in CO_2 methanation, after activation in H_2.

2.2. Preparation of the Ru/TiO_2 methanation catalysts

To prepare Ru-based catalysts, mesoporous TiO_2 samples were impregnated with pre-synthesized RuO_2 nanoparticles. The preparation of the aqueous colloidal suspension of 2 nm RuO_2 by reaction of $RuCl_3$ with H_2O_2 is described elsewhere.[49-50] This suspension had a Ru concentration 0.007 M. First, certain amount (2 g to 12 g) of mesoporous TiO_2 was added to a precise volume of RuO_2 nanoparticles colloidal suspension to yield 2.2 wt. % of Ru in the final catalyst, then the mixture was put in an ultrasonic bath for 30 minutes operating at 40 kHz at room temperature. This step was introduced in attempt to separate agglomerated mesoporous spheres as well as to favor the diffusion of RuO_2 nanoparticles inside the pores. Then, water was evaporated by rotary evaporation under vacuum at 50 °C. The resulting dried powder was annealed at various temperatures (350, 450, 550, or 650 °C) for 4 h with a 10 °C/min heating ramp. The obtained catalysts are denoted "TiXRuY", where X corresponds to the temperature of calcination for the titania support and where Y represents the annealing temperature after RuO_2 nanoparticles deposition (Table 1).

Table 1. List of the samples, thermal treatments applied, and textural properties (N_2-physisorption).

	Sample	Calcination T (°C)[a]	Annealing T (°C)[b]	SSA_{BET} ($m^2.g^{-1}$)	D_p (nm)	V_p ($cm^3.g^{-1}$)	Methanation activity ($\mu mol_{CH4}.g_{cat}^{-1}.s^{-1}$)
Supports	Ti325	325	N/A	310	5.4	0.43	N/A
	Ti350	350	N/A	260	5.4	0.36	N/A
	Ti375	375	N/A	210	5.5	0.30	N/A
	Ti400	400	N/A	160	6.4	0.25	N/A
	Ti425	425	N/A	130	6.8	0.22	N/A
	Ti450	450	N/A	130	6.8	0.23	N/A
Catalysts	Ti350Ru350	350	350	166	6.7	0.28	0.86
	Ti350Ru450	350	450	112	8.7	0.24	2.05
	Ti350Ru550	350	550	69	11.0	0.19	1.62
	Ti350Ru650	350	600	29	17.7	0.13	1.46

[a] Performed to remove the surfactant and release the mesoporosity in the TiO_2 support

[b] Performed to anneal RuO_2 nanoparticles on the TiO_2 support. Such annealing before reduction is needed to get high methanation activity.[21]

2.3. Characterization

The specific surface area of the catalysts was obtained from the nitrogen physisorption isotherms collected at −196 °C on a BELSORB-mini II (BEL Japan, Inc.). The samples were outgassed overnight at 140 °C prior to the analysis. Specific surface area (S_{BET}) was calculated applying the Brunauer-Emmet-Teller (BET) method for N_2 relative pressure in the $0.05 < P/P_0 < 0.30$ range. Total pore volume (V_p) was measured at $P/P_0 \sim 0.98$. Pore size distribution was determined by the Barret-Joyner-Halenda (BJH) method.

Transmission electron microscopy (TEM) images were obtained with a FEI Tecnai 120 Twin microscope, operating at 120 kV and equipped with a GatanOrius CCD numeric camera. The samples were prepared by ultrasonic dispersion of the powders in water and a droplet of the dispersion was then placed onto a carbon-coated copper grid.

High-resolution analysis (HR-TEM) images were obtained by using a JEOL JEM 2010 microscope, operating at 200 kV and equipped with a Gatan camera. The samples were prepared by embedding of the powders in epoxy resin (Araldite 502) and ultra-thin section of 80nm were sliced with a UC7 Leica ultra-microtome.

X-ray diffraction (XRD) measurements were performed using Cu Kα radiation in a Bruker D8 Advance diffractometer equipped with a Lynx eye detector. The 2θ diffractograms were recorded between 24–50°with a step size of 0.04° and a step time of 20 s/step. The ICDD-PDF2 database was used to identify the crystalline phases. When possible, TiO_2 and RuO_2 XRD peaks were deconvoluted, using WinPLOTR 2014.[51] The Scherrer equation was used to calculate the crystallite size of particles. The same sample holder was always used, with similar quantities of powder and similar packing. This allows us to compare the different diffraction peaks in terms of intensity (surface under the curve) which is related to the quantity of each crystalline phase.

Small-Angle X-ray Scattering (SAXS) experiments were carried out with Rigaku's S-MAX3000 3-pinhole SAXS camera with X-ray source (high brilliance MIcroMax-002) with Copper anode (λ CuKα = 1.54056 Å). The scattering radiation was collected on 2D Multiwire Area Detector (gas detector) with a sample-to-detector distance of 1469 mm.

H_2-Temperature programmed Reduction (TPR) experiments were performed on 100 mg of each catalyst after in situ purging under inert gas (Ar) at 140 °C for one hour. The analysis was carried out under 2.5 v/v % H_2 diluted in inert gases (2.5: 82.5: 15 v/v % H_2: He: Ar) in a stream of 20

mL.min^{-1} from 20 °C to 500 °C using a 5 °C min^{-1} temperature ramp. H_2 consumption and H_2O production were measured simultaneously via a quadrupole mass spectrometer QMC 311 (Balzers) coupled in line with the reactor.

The weight percentages of Ru and Ti inside the catalysts were measured by Inductively Coupled Plasma-Atomic Emission Spectroscopy (ICP-AES) on an ICAP 6500 from Thermo Scientific. To fully solubilize Ti and Ru, ~50 mg of catalyst was mixed with 2 g of sodium peroxide and 1 g of NaOH (tablets) and the mixture was fused in a vitreous carbon crucible in the flame of a Bunsen. The fused mixture was then cooled and plunged in a bath of aqueous HCl (30%).

Fourrier Transformed Infrared (FTIR) spectroscopy was performed on Single reflection horizontal Attenuated Total Reflectance (ATR) accessory from Brucker, diamond crystal plate equipped with high pressure QuickLock. The spectra was recorded with 100 scans between 400 and 4000 cm^{-1} with a resolution of 4 cm^{-1}.

2.4. CO_2 methanation

200 mg of catalyst with particle size between 100 and 315 µm was loaded in a continuous flow fixed bed reactor and reduced in situ at 200 °C for 2 h under 30 ml/min of H_2 prior to the catalytic reaction. The reaction was carried out at 1 atm in the 50-200 °C range under reaction mixture of 20 ml/min (CO_2 (10 vol. %), H_2 (40 vol. %) diluted in He). Each temperature was maintained for ~1 hour (allowing for 3 GC injections). The exit gases were quantified using a gas chromatograph (Varian CP3800), equipped with Hayesep Q, Molsieve 5A, and CP-Sil-5CB columns. The separated gases were detected with a flame ionization detector (CH_4) and a thermal conductivity detector (CO and CO_2). Analysis parameters were set as to allow an analysis each 19 min and to obtain measurements accurate within about 1 % (relative) for the methane production rate (mole

of methane produced per gram of catalyst per second). All transfer lines were maintained at 110 °C to avoid water condensation.

3. Results and discussion

3.1. Preparation of pure mesoporous TiO_2 with tunable texture and structure

Via the "Type IIIc" aerosol process[37] described above, a fresh TiO_2 powder was produced in a continuous mode. The spherical shape of the particles (Figure 2) is a reminiscence of the liquid droplets from which the particles originate. The particles are dense, with pores in close-packing down to the core of the spheres. When the calcination temperature was relatively low (e.g. Ti350), the particle surface appeared smooth and the mesostructure was clearly visible, with uniform pore size of ~5 nm. When the calcination was relatively high (e.g. Ti450) the growth of TiO_2 grains was observed, together with the partial destruction of the mesostructure. Yet, the global shape of the aerosol droplets was fairly well-preserved.

The porosity is generated by the presence of a structure-directing triblock copolymer (F127) which undergoes evaporation-induced self-assembly during the aerosol processing, generating micelles around which the inorganic polycondensation takes place (Figure 1). The removal of the surfactant is needed to obtain mesoporous TiO_2 spheres. This is, however, a delicate process due to the amorphous nature of the initially obtained mesostructured TiO_2 spheres. Due to the replacement of hydrolysable alkoxy groups by acetate groups, the degree of cross-linking and the density of the metal gel network is lower than that of bulk TiO_2 materials with a pure oxide framework.[30] As a result, the fresh mesostructured TiO_2 is less-condensed and sustaining the mesoscopic order after removal of the organic template by thermal treatment requires a strategic approach.

The decomposition of pure F127 was analyzed by TGA (Figure S1). F127 was mostly decomposed before 400 °C and almost completely decomposed at 600 °C. The fresh mesostructured TiO_2 material was analyzed under two different conditions: (i) up to 600 °C with a heating rate of 5 °C/min and (ii) up to 350 °C with a heating rate of 1 °C/min followed by a plateau at 350°C for 10 hours (i.e. like the calcination conditions). The decomposition temperature of F127 was slightly shifted towards lower temperature with a decreased heating rate. When the fresh sample was heated up to 350 °C with 1 °C/min and kept at 350 °C for 10 hours, further weight loss was observed only during the first 4.5 hours of the dwell (Fig. S1). This shows that a calcination duration of 5 hours is enough to remove the organic template at maximum at a given calcination temperature. The total weight loss of the fresh sample was about 60 % which is consistent with the composition of non-volatile organic components of the sol that was used in the aerosol-assisted sol-gel process.

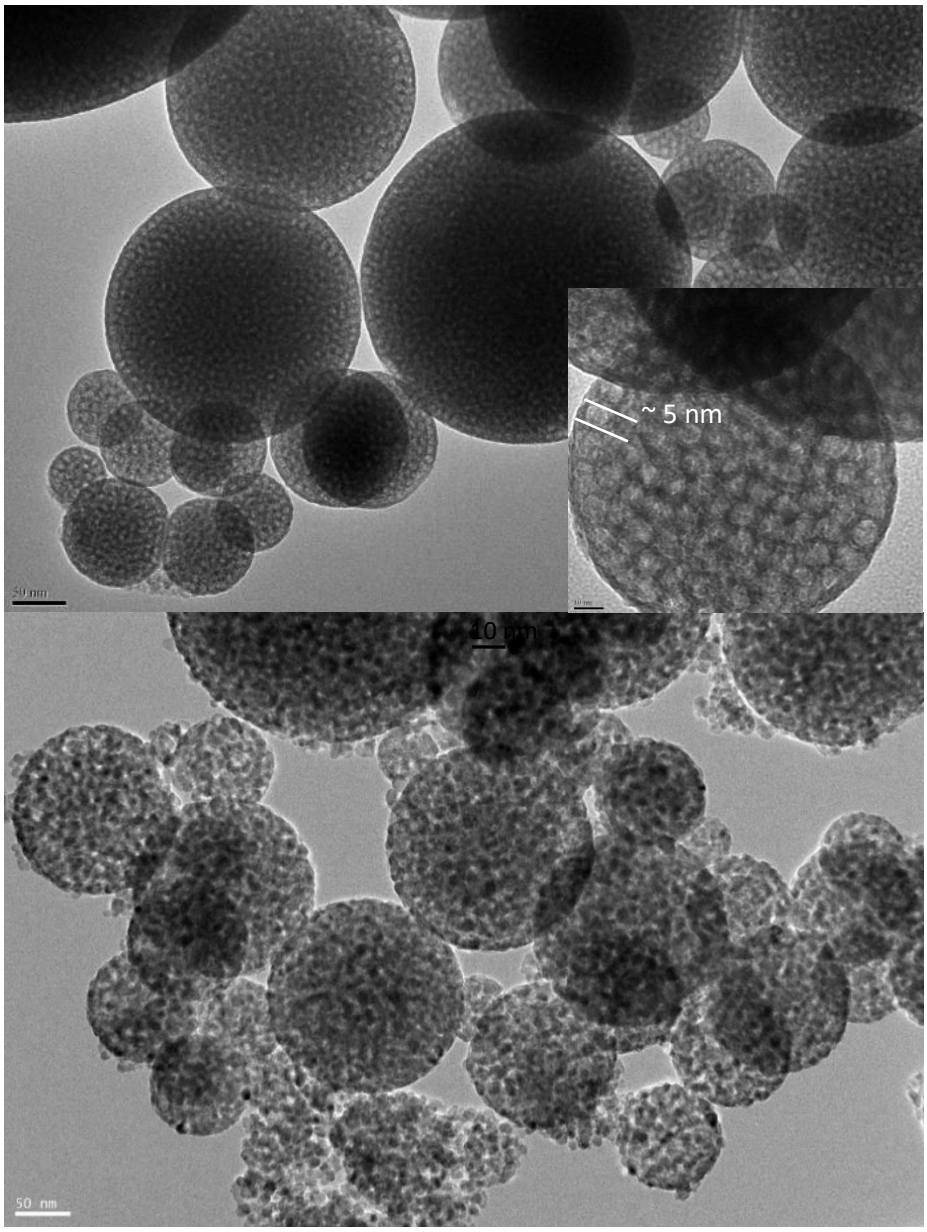


Figure 2. TEM image of Ti350 (top) and Ti450 (bottom); the inset shows a zoomed-in image of Ti350 showing the pore size of 5 nm.

FTIR-ATR analysis was performed on selected samples: pure F127, fresh TiO_2, Ti350, Ti375, Ti425, and Ti450 (Figure 3). Expectedly, the stretching vibration of C-H and C-O-C of PEO and PPO blocks at 2880 cm^{-1} and 1105 cm^{-1} was detected in the fresh TiO_2 aerosols.[52] The removal of F127 after calcination at 350 °C and higher temperatures was confirmed, as these bands

disappeared. The very weak peak observed at 2980 cm^{-1} on all samples is related to C-H asymmetric stretching[53] and can be attributed to the presence of organic impurities. The broad bands around 3300 cm^{-1} and 1630 cm^{-1} are assigned to stretching and bending vibration modes of adsorbed water molecules.[54] For calcined materials, the broad band centered around 715 cm^{-1} and the weak band at 410 cm^{-1} are associated to Ti-O-Ti vibrations.[54] These bands, however, were slightly shifted towards higher wavenumber (at 790 cm^{-1} and 440 cm^{-1}) when the support was calcined at 350°C only (Ti350). The peak around 800 cm^{-1} is assigned to Ti-O vibration, where the oxygen atom is in the non-binding condition.[55] This can be associated with the lower degree of TiO_2 lattice formation after calcination at 350 °C compared to higher temperature-calcined samples.[54, 56]

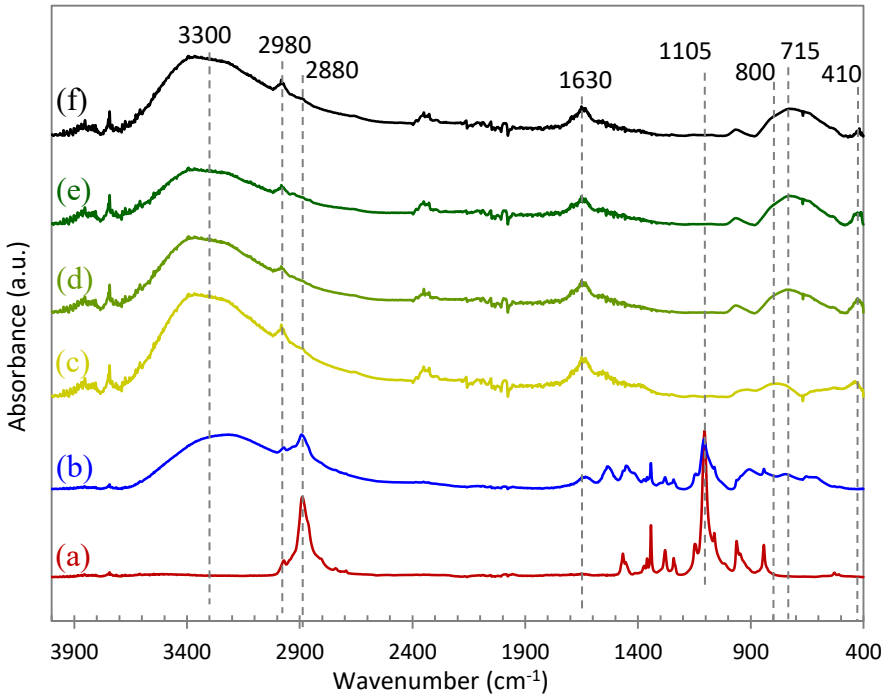


Figure 3. FTIR-ATR spectra of (a) F127, (b) fresh mesostructured sample, and 5x amplified spectra of (c) Ti350, (d) Ti375, (e) Ti425, and (f) Ti450; dotted lines are guide to the eyes.

Calcination of the support had a dramatic impact on the textural properties of the obtained mesoporous TiO_2 (Table 1). At 325°C, the specific surface area and the total pore volume reached 310 $m^2.g^{-1}$ and 0.43 $cm^3.g^{-1}$ respectively, which is remarkable for pure TiO_2 materials.[36, 57] The specific surface area (SSA) decreased linearly with increasing calcination temperature between 325°C and 425°C. At 450°C however, the SSA did not decrease further. The pore volume followed the same trend. These trends can be visualized in Figure S2.

The N_2 physisorption isotherms of all samples belong to type IV, with a characteristic hysteresis loop associated with the presence of open mesopores (Figure 4). The shape of the hysteresis loops corresponds to H2 type (asymmetrical with a steeper desorption branch than the adsorption branch) characteristic of restrictions within the porous network. With increasing calcination temperature, N_2 desorption appears at higher partial pressure and is less steep, which corresponds to less defined pore size and shape or to more interconnected pores.[58] So, the observed modifications of the isotherms are consistent with the fact that channel-like pores created by the removal of calibrated cylindrical micelles are progressively replaced by pores formed as the interstices between TiO_2 crystals.

Pore size distribution was centered around 3-5 nm for the support calcined at relatively low temperature (Figure 4). This size is consistent with the expected size of the micelles formed by F127.[48] The pore size distribution became broader and shifted to larger sizes after calcination at 400°C and higher, consistent with a progressive disruption of the mesoscopic order when calcination temperature increases.

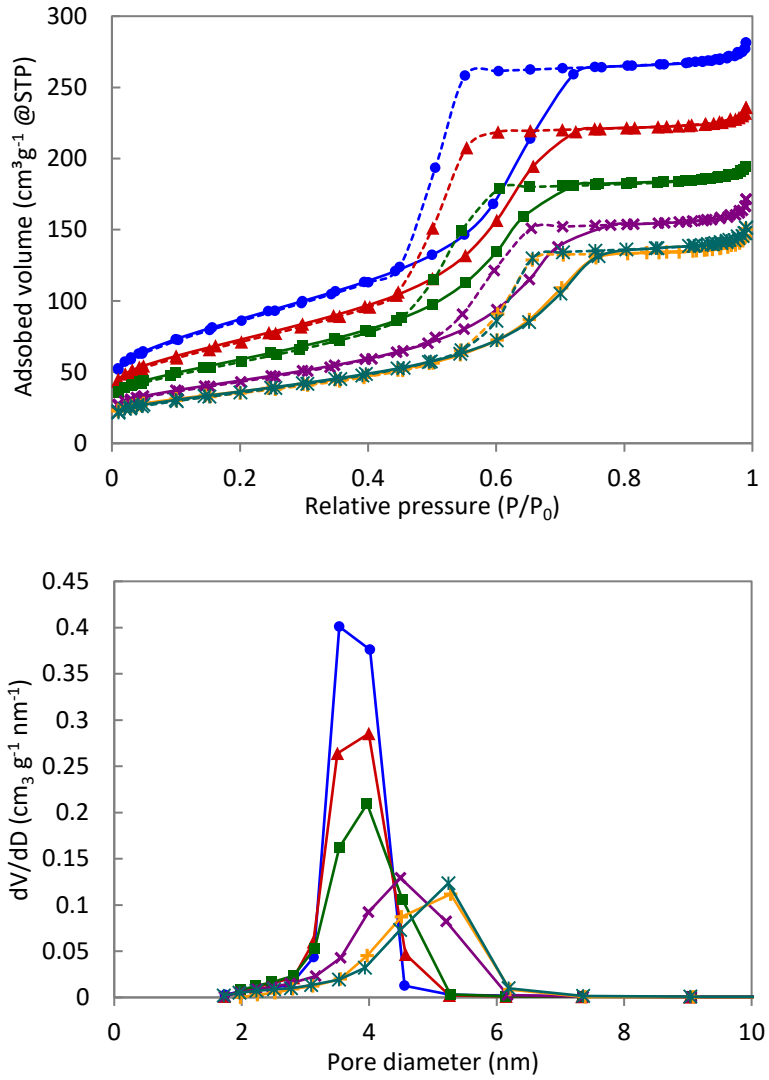


Figure 4. N_2 physisorption analyses: (top) N_2-physisorption isotherms and (bottom) BJH pore size distribution of Ti325 (●), Ti350 (▲), Ti375 (■), Ti400 (✖), Ti425 (✚), and Ti450 (✳). Adsorption isotherms are plotted in plain lines and desorption isotherms are plotted in dashed lines.

XRD analysis revealed the onset of the TiO_2 anatase phase already starting at the calcination temperature of 350 °C (Figure 5). The crystal growth is more pronounced as the calcination temperature increases. This confirms that the amorphous mesoporous walls are progressively being converted into aggregates of growing anatase crystallites.

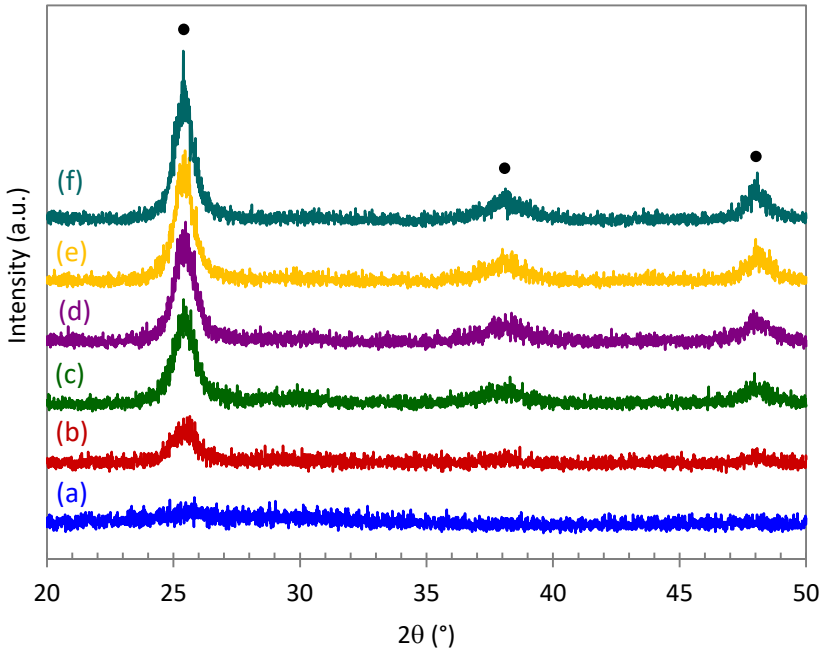


Figure 5. XRD patterns of (a) Ti325, (b) Ti350, (c) Ti400, (d) Ti375, (e) Ti425, and (f) Ti450. Black dots indicate anatase TiO_2 crystal planes; black dot (●) indicates anatase TiO_2 phase.

From SAXS analysis, a correlation peak which indicates the mesoscopic order in the sample was found in the case of the fresh and 350 °C calcined samples (Figure S3). The d-spacing, which corresponds to the distance between the repeating unit (wall-to-wall distance) was calculated ($d = 2\pi/q$) to be 11.4 nm and 8.4 nm for the fresh sample and Ti350, respectively. The decrease in the d-spacing after calcination is attributed to the shrinkage due to the densification of the TiO_2 network. Based on the pore diameter observed by TEM and N_2 physisorption analysis for Ti350 (approximately 5 nm), the TiO_2 wall thickness is estimated to be 3 to 4 nm. On the other hand, no correlation peak was observed after calcination at 375 °C and higher. This further indicates the destruction of the mesostructure due to the growth of the anatase phase.

Overall, the employed aerosol-assisted sol-gel process led to spherical TiO_2 particles with mesopores released by the efficient removal of the surfactant. The textural properties and the

crystallinity of the support can be tuned by selecting the appropriate calcination temperature. In the following, the mesoporous TiO_2 material obtained after calcination at 350 °C (Ti350) was chosen as a starting support since it maintained the mesostructure with high specific surface area and well-defined pore size, without significant crystal growth after calcination.

3.2. RuO_2/TiO_2 catalysts prepared by the impregnation of RuO_2 NP onto mesoporous TiO_2

Ti350 was impregnated with a suspension of ~2 nm sized RuO_2 nanoparticles[49, 59] so as to reach a loading of 2.2 wt.% of Ru (the experimental Ru loading was between 2.0 and 2.3 wt., as verified by ICP-AES on selected catalysts; not shown). The catalyst was further annealed at different temperatures under static air.

Clearly, the introduction of Ru species combined with further annealing affected the texture of the starting mesoporous TiO_2, even when the annealing temperature of the catalysts was the same as the calcination temperature of the pure mesoporous TiO_2 (Table 1 and Figure 6). As expected, the surface area and the pore volume decreased with higher annealing temperatures, whereas the average pore diameter was increased which indicates the progressive destruction of the mesoscopic order. Yet, all catalysts still presented type IV isotherms characteristic of mesoporous materials, maintaining the shape of the hysteresis loop.

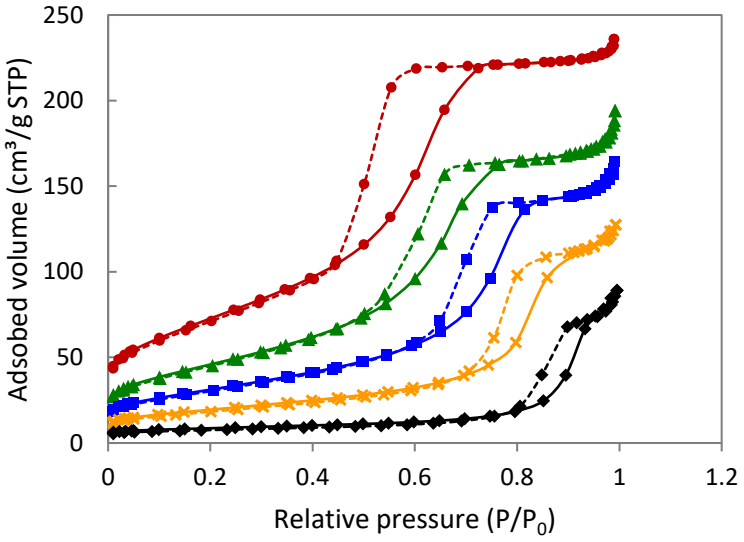


Figure 6. N_2 isotherms of Ti350 (●), Ti350Ru350 (▲), Ti350Ru450 (■), Ti350Ru550 (✖), and Ti350Ru650 (◆). Adsorption isotherm is in plain lines and desorption isotherm is in dashed lines.

The XRD patterns of the catalysts annealed at different temperatures are presented in Figure 7 and the XRD peaks were deconvoluted using WinPlotR software to obtain precise positions and widths of TiO_2 and RuO_2 phases between 34 and 42 in 2 theta (Fig. S3 and Table S1). While the bare support calcined at 350°C showed only weak signals of anatase TiO_2, further crystallization and growth of this anatase phase was observed upon annealing in the presence of Ru species. Interestingly, the (110) and (101) peaks of rutile TiO_2 (ICDD 00-021-1276**)** were also detected starting at the very low 250°C annealing temperature. Looking at the evolution of the amount of each phase as a function of annealing temperature (Figure S4) it appears that rutile TiO_2 and anatase TiO_2 both increase from 250 to 450°C, indicating that the crystallization of the amorphous TiO_2 solid takes place during annealing. Rutile TiO_2 amount further increases over 450°, while the anatase amount reaches a maximum at 450°C and then decreases, pointing to the occurrence of the anatase to rutile transition.[60-61] In fact, amorphous TiO_2[62-63] or anatase or brookite[64] phases are known to undergo a non-reversible phase transition towards rutile when heated at high

temperature, rutile TiO_2 being the thermodynamic phase. This solid-solid transition usually occurs between 400 to 700°C, depending on several criterions such as particle size, purity, atmosphere, etc. Here, the amorphous to rutile TiO_2 transition starts as low as 250°C, which is to our knowledge unprecedented. It clearly appears to be triggered by the presence of RuO_2 nanoparticles, because the rutile TiO_2 phase did not form when bare Ti350 was further annealed at 550 °C, in the same condition as Ti350Ru550 (XRD pattern not shown). It should be noted that the 2 nm impregnated RuO_2 nanoparticles are crystalline,[49] yet their size prevent any diffraction phenomena to occur. Sintering at higher temperature is responsible for RuO_2 peak appearance.

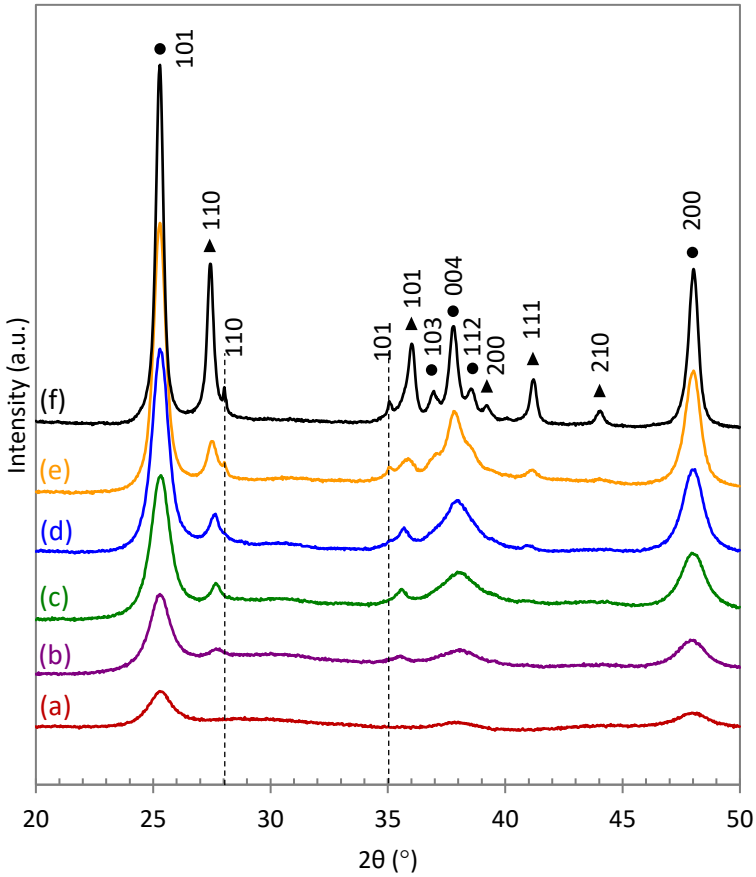


Figure 7. XRD patterns of (a) Ti350, (b) Ti350Ru250, (c) Ti350Ru350, (d) Ti350Ru450, (e) Ti350Ru550, and (f) Ti350Ru650. Peak positions: (▲) rutile TiO_2, (●) anatase TiO_2, (dotted lines) rutile RuO_2.

Interestingly, at low annealing temperature, the (110) TiO_2 rutile peaks appears shifted towards high angles, while the (101) peaks are shifted towards low angles (as compared to the reference for rutile TiO_2). Rutile TiO_2 peaks are thus closer to the RuO_2 peak positions. In the meantime, RuO_2 peaks are distinguished from 450°C (Figure S5); their positions are perfectly centered on the known ICDD 01-070-2662 RuO_2 reference. As the annealing temperature increases, the positions of RuO_2 peaks remained constant while the positions of rutile TiO_2 peaks, evolved towards the expected positions for rutile TiO_2 (Figure 8). This phenomenon is a proof that the rutile TiO_2 phase was seeded by the impregnated 2 nm RuO_2 nanoparticles. In fact, Rutile TiO_2 has already been reported to crystallize from anatase at 350°, in the presence of RuO_2.[21] The degree of mismatch between RuO_2 (ICDD 01-070-2662) and rutile TiO_2 (ICDD 00-021-1276) is only of 1.8% for (110) and 2.7% for (101), largely below the generally accepted 5% authorized limit for epitaxial growth. Thus, the growth of rutile TiO_2 layer was also reported to be promoted by using RuO_2 as a seed layer for the fabrication of RuO_2-TiO_2 films, using the epitaxial match between the rutile RuO_2 and rutile TiO_2.[65-66] This epitaxial relation between (101) TiO_2 and (101) RuO_2 becomes weaker as the size of the particles increases (and surface decrease) with increasing annealing temperature. The Scherrer calculations confirmed the growth of RuO_2 crystallites with increased annealing temperature; 29 nm (450°C), 38 nm (550°C), to 68 nm (650°C) for (110) RuO_2 and 13 nm (450°C), 12 nm (550°C), to 22 nm (650°C) for (101) RuO_2.

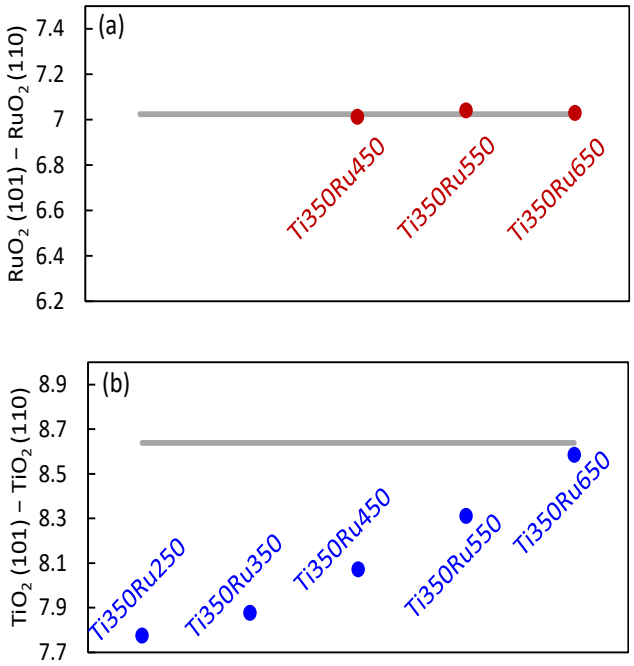


Figure 8. Difference between 101 and 110 peak positions for (a) rutile RuO_2 and (b) rutile TiO_2. The grey lines represent the expected value based on ICDD 01-070-2662 for RuO_2 and ICDD 00-021-1276 for TiO_2. The complete XRD data set (peak position and width after deconvolution) is available in Table S1.

HR-TEM was performed on Ultra-thin sections of spent Ru350Ti350 samples. This way, Ru species are reduced, which allows a better Ru/TiO_2 contrast and thus easier detection. The location of Ru species allows us to define the location of RuO_2 since it has already been established that no Ru species migration occurs during reduction or methanation.[21] Ru was clearly detected inside the spheres, proving that RuO_2 nanoparticles had indeed the possibility to diffuse inside the mesoporous network of the support during impregnation (Figure 9). A certain accumulation of Ru nanoparticles was also noticed, forming domains of about 40 nm wide in which higher concentration of small Ru nanoparticles ranging from 2 to 5 nm are visible. This shows that a partial but limited sintering of RuO_2 could not be avoided. This can be related to previous observations highlighting the substantial sintering of RuO_2 particles when deposited onto

anatase.[21] Upon annealing at higher temperature (Ru350Ti450) the HR-TEM images showed that the Ru species were always present within the TiO_2 support, and not separated from the TiO_2 microspheres (Figure 9). Rutile TiO_2 phase was observed in close proximity to Ru species, as expected from X-Ray analyses. The size of Ru aggregates observed in HR-TEM is in accordance with the RuO_2 size estimated from Scherrer calculations.

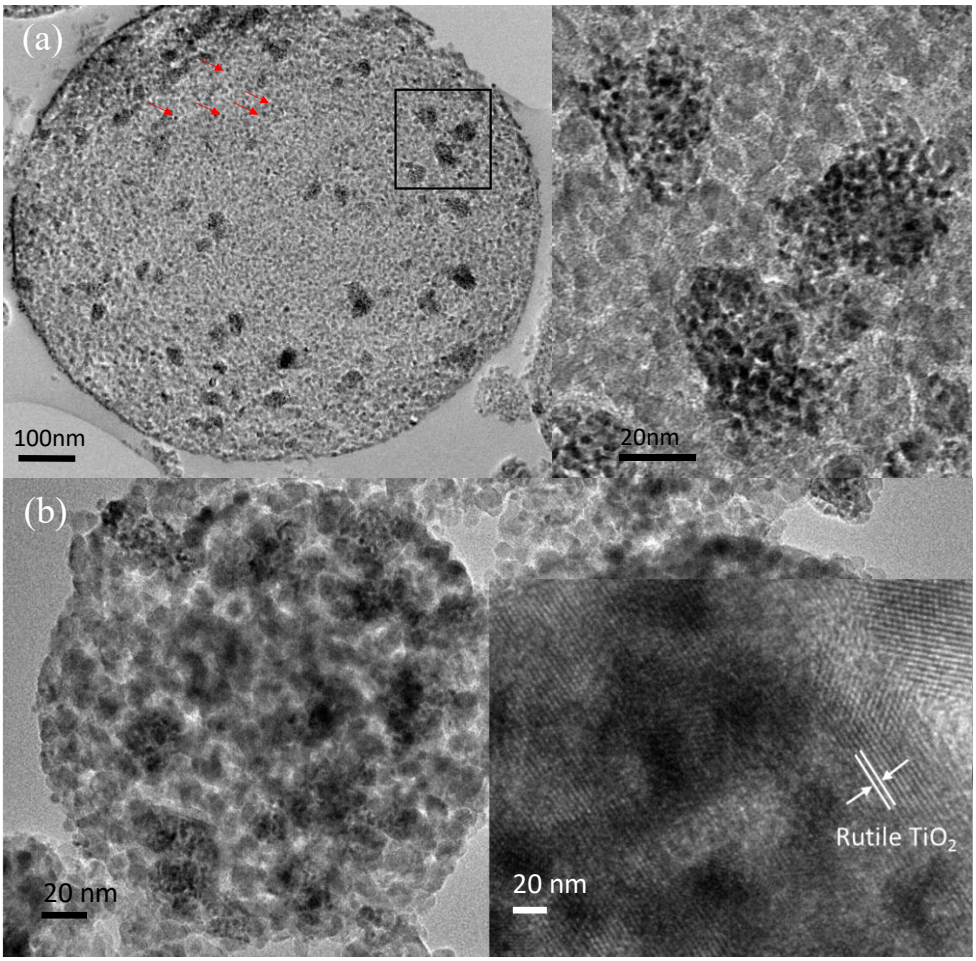


Figure 9. (a) HR-TEM performed on an ultra-thin section of spent Ru350Ti350 catalyst (red arrows show isolated Ru nanoparticles; larger aggregates are clearly visible, and highlighted in the inset). (b) HR-TEM on the spent Ti350Ru450 catalyst (the inset shows the crystal planes of rutile TiO_2 close to the Ru aggregates).

FTIR-ATR analysis after RuO_2 deposition and further annealing is shown in Figure S6. The weak bands in the 800 – 400 cm^{-1} range became more prevalent for the further annealed catalysts compared to Ti350. Specifically, the maxima of the peaks at 790 cm^{-1} and 440 cm^{-1} shifted towards lower wavenumber, which can be attributed to the strengthening of the TiO_2 network.[54, 56]

H_2-TPR experiments were carried out on selected samples after RuO_2 deposition. The shape of the reduction profile was different depending on the annealing temperature (Figure S7). A small reduction peak was observed around 125 °C for Ti350Ru350 suggesting that some residual Ru^{3+} species from the colloidal suspension may still be present after annealing at 350 °C.[67] The main reduction event occurred at higher temperature and tended to shift towards higher temperatures with higher annealing temperature. This can be attributed to a lower reducibility of the larger RuO_2 particles detected by XRD.

3.3. CO_2 methanation

The catalysts were activated in situ in a pure hydrogen feed at 200 °C before being tested in the CO_2 methanation reaction up to 200 °C. N_2 physisorption analyses after in situ reduction and methanation reaction showed that the textural properties remained unchanged (not shown). For all catalysts discussed here, the activity was stable in time and the selectivity to methane was 100%, as classically observed with Ru-based catalysts at 200°C or lower.[21] The absence of external and internal diffusion limitations was verified (see ESI and Figure S8). Also, the reaction conditions were set as to obtain relatively low conversion levels, far away from the thermodynamic equilibrium, ensuring that the reported rates correspond to the intrinsic specific activity. The methane production rates is expressed as μmol of methane produced per gram of catalyst and per second.

For the catalysts annealed at various temperatures the methanation production rate is relatively low after annealing at 350°C but reached a maximum after annealing at 450 °C, and decreased after annealing at 550 °C or higher temperature (Table 1 and Figure S9). The most active catalyst (Ti350Ru450) reached a methane production rate of 2.05 µmol of methane per gram of catalyst and per second. Comparing with other catalysts with the same Ru loading and tested in the same conditions, this is slightly lower than the rate reported when a non-sintering rutile-TiO_2 support was used (3.5 $\mu mol_{CH4}\ g_{cat}^{-1}\ s^{-1}$)[20] but in the same order as the rates reported for Ru/TiO_2 prepared Degussa-P25 as a support (2.6 $\mu mol_{CH4}\ g_{cat}^{-1}\ s^{-1}$).[21]

Several parameters determine the final stability and activity of Ru/TiO_2 methanation catalysts: crystalline structure (of the support and of the ruthenium phase), sintering (support or/and ruthenia), migration of RuO_2 species towards rutile TiO_2, phases stabilization, modification of porosity or surface accessibility, dispersion or aggregation of the active phase, phase transition, etc. For non-sintering TiO_2 supports, rutile TiO_2 was shown to be the most effective support to prepare highly active Ru/TiO_2 methanation catalysts.[21] The strong epitaxy link between TiO_2 rutile and RuO_2 led to the best RuO_2 dispersion on TiO_2 surface, and thus after reduction, to well dispersed Ru particles. In the case of mixtures between anatase and rutile, it is the amount of accessible rutile that drives the activity. Here we show that it is possible to trigger TiO_2 rutile crystallization, benefitting from the seeding action of RuO_2 nanoparticles and keeping a mesoporous material. The increase of activity between 350°C and 450°C annealing can be seen as the consequence of the increase in the amount of rutile TiO_2 particles. Unfortunately, with further heating, a strong decrease in porosity is provoked by a heavier TiO_2 and RuO_2 sintering, which appears to limit the catalytic activity.

4. Conclusion

Mesostructured TiO_2 materials were successfully synthesized via an aerosol-assisted sol-gel process. The resulting TiO_2 powders could be obtained with a good control on the textural properties upon removal of the organic template. Crystallization of amorphous TiO_2 to crystalline anatase phase was inevitable especially after calcination at 350 °C and higher temperatures. These modifications resulted in patent textural modifications that are however controllable to a certain extent by selecting the calcination temperature. The mesoscopic order was maintained after calcination at 350 °C with well-defined pore size of 5 nm and specific surface area of 260 $m^2.g^{-1}$. It was progressively disrupted when higher calcination temperature were used.

The 350°C-calcined mesoporous TiO_2 support was used as support for RuO_2 nanoparticles to serve as a catalyst containing 2.2 wt. % Ru for CO_2 methanation. Ru-species were found inside the pores of TiO_2 support after in situ reduction and reaction, showing that a simple impregnation of the mesoporous support with an aqueous suspension of RuO_2 nanoparticles is suitable. The annealing of the partially oxidized Ru-species was found to be an important activation step as the catalytic activity was at its maximum when annealed at 450 °C. The RuO_2 nanoparticles promoted further modifications of the low crystalline TiO_2 support materials during annealing. On the one hand, the growth of the rutile TiO_2 phase was triggered at annealing temperature as low as 250 °C, due to the close structural similarities of RuO_2 and rutile TiO_2 (epitaxy). On the other hand, the amorphous materials is mainly crystallized in the anatase phase, which favors the buildup of large RuO_2 aggregates. Globally, these catalysts did not outcompete the reference prepared from non-sintering rutile TiO_2 supports. This study allows us to observe the beneficial role of rutile TiO_2 structure to stabilize RuO_2, maintain good dispersion, and trigger high catalytic activity.

Acknowledgements

A.K. thanks the European doctoral school IDS FunMat fort the PhD fellowship. The authors acknowledge *Wallonie-Bruxelles International*, the *Ministère Français des Affaires étrangères et européennes* and the *Ministère de l'Enseignement Supérieur et de la Recherche* for their financial support in the framework of the Hubert Curien partnership (Tournesol). F.R.S.–FNRS is thanked for the acquisition of the physi-chemisorption equipment used here (project "EQP U.N030.18"). Authors also acknowledge the *Fondation Collège de France*. The Francqui Foundation is thanked for the grant which made it possible for Professor Sanchez to visit Belgium.

Supporting information for this article presents a schematic view of the aerosol set-up, TGA and SAXS results for the TiO_2 materials calcined at different temperatures, detailed XRD diffractograms for RuO_2/TiO_2 catalysts (along with a comprehensive table for position and FWHM after deconvolution), FTIR spectra for supports and catalysts, TPR profiles for catalysts, and a discussion on the validity of the activity measurements.

References

1. Mikkelsen, M.; Jorgensen, M.; Krebs, F. C., The teraton challenge. A review of fixation and transformation of carbon dioxide. *Energ. Env. Sci.* 2010, *3* (1), 43-81.

2. Wang, W.; Wang, S.; Ma, X.; Gong, J., Recent advances in catalytic hydrogenation of carbon dioxide. *Chem. Soc. Rev.* 2011, *40* (7), 3703-3727.

3. Aziz, M. A. A.; Jalil, A. A.; Triwahyono, S.; Ahmad, A., CO2 methanation over heterogeneous catalysts: recent progress and future prospects. *Green Chem.* 2015, *17* (5), 2647-2663.

4. Frontera, P.; Macario, A.; Ferraro, M.; Antonucci, P., Supported Catalysts for CO2 Methanation: A Review. *Catalysts* 2017, *7* (2), 59.

5. Wei, W.; Jinlong, G., Methanation of carbon dioxide: an overview. *Frontiers Chem. Sci. Eng.* 2011, *5* (1), 2-10.

6. Marques Mota, F.; Kim, D. H., From CO2 methanation to ambitious long-chain hydrocarbons: alternative fuels paving the path to sustainability. *Chem. Soc. Rev.* 2019, *48* (1), 205-259.

7. Buttler, A.; Spliethoff, H., Current status of water electrolysis for energy storage, grid balancing and sector coupling via power-to-gas and power-to-liquids: A review. *Renewable and Sustainable Energy Reviews* 2018, *82*, 2440-2454.

8. Melo, P.; Debecker, D. P., Combining CO_2 capture and catalytic conversion to methane. *Waste Disposal & Sustainable Energy (In Press)* 2019, DOI:10.1007/s42768-019-00004-0.

9. Carenco, S.; Sassoye, C.; Faustini, M.; Eloy, P.; Debecker, D. P.; Bluhm, H.; Salmeron, M., The Active State of Supported Ruthenium Oxide Nanoparticles during Carbon Dioxide Methanation. *J. Phys. Chem. C* 2016, *120* (28), 15354-15361.

10. Martins, J.; Batail, N.; Silva, S.; Rafik-Clement, S.; Karelovic, A.; Debecker, D. P.; Chaumonnot, A.; Uzio, D., CO2 hydrogenation with shape-controlled Pd nanoparticles embedded in mesoporous silica: Elucidating stability and selectivity issues. *Catal. Commun.* 2015, *58*, 11-15.

11. Mebrahtu, C.; Abate, S.; Perathoner, S.; Chen, S.; Centi, G., CO2 methanation over Ni catalysts based on ternary and quaternary mixed oxide: A comparison and analysis of the structure-activity relationships. *Catal. Today* 2018, *304*, 181-189.

12. Shin, H. H.; Lu, L.; Yang, Z.; Kiely, C. J.; McIntosh, S., Cobalt Catalysts Decorated with Platinum Atoms Supported on Barium Zirconate Provide Enhanced Activity and Selectivity for CO2 Methanation. *ACS Catal.* 2016, *6* (5), 2811-2818.

13. Bacariza, M. C.; Bértolo, R.; Graça, I.; Lopes, J. M.; Henriques, C., The effect of the compensating cation on the catalytic performances of Ni/USY zeolites towards CO2 methanation. *J. CO2 Utilization* 2017, *21*, 280-291.

14. Garbarino, G.; Wang, C.; Cavattoni, T.; Finocchio, E.; Riani, P.; Flytzani-Stephanopoulos, M.; Busca, G., A study of Ni/La-Al2O3 catalysts: A competitive system for CO2 methanation. *Appl. Catal. B* 2019, *248*, 286-297.

15. Arandiyan, H.; Kani, K.; Wang, Y.; Jiang, B.; Kim, J.; Yoshino, M.; Rezaei, M.; Rowan, A. E.; Dai, H.; Yamauchi, Y., Highly Selective Reduction of Carbon Dioxide to Methane on Novel Mesoporous Rh Catalysts. *ACS Appl. Mater. Interfaces* 2018, *10* (30), 24963-24968.

16. Solymosi, F.; Erdohelyi, A.; Kocsis, M., Methanation of CO2 on supported Ru catalysts. *J. Chem. Soc. Faraday Trans.* 1981, *77* (5), 1003-1012.

17. Wang, F.; He, S.; Chen, H.; Wang, B.; Zheng, L.; Wei, M.; Evans, D. G.; Duan, X., Active Site Dependent Reaction Mechanism over Ru/CeO2 Catalyst toward CO2 Methanation. *J. Am. Chem. Soc.* 2016, *138* (19), 6298-6305.

18. Abe, T.; Tanizawa, M.; Watanabe, K.; Taguchi, A., CO2 methanation property of Ru nanoparticle-loaded TiO2 prepared by a polygonal barrel-sputtering method. *Energ. Env. Sci.* 2009, *2* (3), 315-321.

19. Abdel-Mageed, A. M.; Widmann, D.; Olesen, S. E.; Chorkendorff, I.; Biskupek, J.; Behm, R. J., Selective CO Methanation on Ru/TiO2 Catalysts: Role and Influence of Metal–Support Interactions. *ACS Catal.* 2015, *5* (11), 6753-6763.

20. Kim, A.; Debecker, D. P.; Devred, F.; Dubois, V.; Sanchez, C.; Sassoye, C., CO2 methanation on Ru/TiO2 catalysts: On the effect of mixing anatase and rutile TiO2 supports. *Appl. Catal. B* 2018, *220*, 615-625.

21. Kim, A.; Sanchez, C.; Patriarche, G.; Ersen, O.; Moldovan, S.; Wisnet, A.; Sassoye, C.; Debecker, D. P., Selective CO2 methanation on Ru/TiO2 catalysts: unravelling the decisive role of the TiO2 support crystal structure. *Catal. Sci. Technol.* 2016, *6* (22), 8117-8128.

22. Lin, Q.; Liu, X. Y.; Jiang, Y.; Wang, Y.; Huang, Y.; Zhang, T., Crystal phase effects on the structure and performance of ruthenium nanoparticles for CO2 hydrogenation. *Catal. Sci. Technol.* 2014, *4* (7), 2058-2063.

23. Wang, D.; Huang, J.; Liu, F.; Xu, X.; Fang, X.; Liu, J.; Xie, Y.; Wang, X., Rutile RuO2 dispersion on rutile and anatase TiO2 supports: The effects of support crystalline phase structure on the dispersion behaviors of the supported metal oxides. *Catal. Today* 2019, DOI:10.1016/j.cattod.2019.02.038.

24. Ward, D. A.; Ko, E. I., Preparing Catalytic Materials by the Sol-Gel Method. *Ind. Eng. Chem. Res.* 1995, *34* (2), 421-433.

25. Debecker, D. P., Innovative Sol-Gel Routes for the Bottom-up Preparation of Heterogeneous Catalysts. *Chem. Record* 2018, *18* (7-8), 662-675.

26. Sanchez, C.; Rozes, L.; Ribot, F.; Laberty-Robert, C.; Grosso, D.; Sassoye, C.; Boissiere, C.; Nicole, L., "Chimie douce": A land of opportunities for the designed construction of functional inorganic and hybrid organic-inorganic nanomaterials. *C. R. Chimie* 2010, *13* (1-2), 3-39.

27. Danks, A. E.; Hall, S. R.; Schnepp, Z., The evolution of 'sol-gel' chemistry as a technique for materials synthesis. *Mater. Horiz.* 2016, *3* (2), 91-112.

28. Ciriminna, R.; Fidalgo, A.; Pandarus, V.; Béland, F.; Ilharco, L. M.; Pagliaro, M., The Sol–Gel Route to Advanced Silica-Based Materials and Recent Applications. *Chem. Rev.* 2013, *113* (8), 6592-6620.

29. Livage, J.; Henry, M.; Sanchez, C., Sol-gel chemistry of transition metal oxides. *Prog. Solid State Chem.* 1988, *18* (4), 259-341.

30. Fan, J.; Boettcher, S. W.; Stucky, G. D., Nanoparticle Assembly of Ordered Multicomponent Mesostructured Metal Oxides via a Versatile Sol−Gel Process. *Chem. Mater.* 2006, *18* (26), 6391-6396.

31. Schubert, U., Chemical modification of titanium alkoxides for sol–gel processing. *J. Mater. Chem.* 2005, *15* (35-36), 3701-3715.

32. Doeuff, S.; Henry, M.; Sanchez, C.; Livage, J., Hydrolysis of titanium alkoxides: Modification of the molecular precursor by acetic acid. *J. Non-Cryst. Solids* 1987, *89* (1), 206-216.

33. Debecker, D. P.; Mutin, P. H., Non-hydrolytic sol-gel routes to heterogeneous catalysts. *Chem. Soc. Rev.* 2012, *41* (9), 3624-3650.

34. Niederberger, M., Nonaqueous Sol–Gel Routes to Metal Oxide Nanoparticles. *Acc. Chem. Res.* 2007, *40* (9), 793-800.

35. Styskalik, A.; Skoda, D.; Barnes, C.; Pinkas, J., The Power of Non-Hydrolytic Sol-Gel Chemistry: A Review. *Catalysts* 2017, *7* (6), 168.

36. Tsung, C.-K.; Fan, J.; Zheng, N.; Shi, Q.; Forman, A. J.; Wang, J.; Stucky, G. D., A General Route to Diverse Mesoporous Metal Oxide Submicrospheres with Highly Crystalline Frameworks. *Angew. Chem. Int. Ed.* 2008, *47* (45), 8682-8686.

37. Debecker, D. P.; Le Bras, S.; Boissiere, C.; Chaumonnot, A.; Sanchez, C., Aerosol processing: a wind of innovation in the field of advanced heterogeneous catalysts. *Chem. Soc. Rev.* 2018, *47*, 4112-4155.

38. Lu, Y. F.; Fan, H. Y.; Stump, A.; Ward, T. L.; Rieker, T.; Brinker, C. J., Aerosol-assisted self-assembly of mesostructured spherical nanoparticles. *Nature* 1999, *398* (6724), 223-226.

39. Boissiere, C.; Grosso, D.; Chaumonnot, A.; Nicole, L.; Sanchez, C., Aerosol Route to Functional Nanostructured Inorganic and Hybrid Porous Materials. *Adv. Mater.* 2011, *23* (5), 599-623.

40. Debecker, D. P.; Stoyanova, M.; Colbeau-Justin, F.; Rodemerck, U.; Boissière, C.; Gaigneaux, E. M.; Sanchez, C., One-pot Aerosol Route to MoO3-SiO2-Al2O3 Catalysts with Ordered Super-Microporosity and High Olefin Metathesis Activity. *Angew. Chem. Int. Ed.* 2012, *51* (9), 2129–2131.

41. Kuai, L.; Wang, J.; Ming, T.; Fang, C.; Sun, Z.; Geng, B.; Wang, J., Aerosol-spray diverse mesoporous metal oxides from metal nitrates. *Sci. Rep.* 2015, *5*, 9923.

42. Smeets, V.; Boissière, C.; Sanchez, C.; Gaigneaux, E. M.; Peeters, E.; Sels, B. F.; Dusselier, M.; Debecker, D. P., Aerosol route to TiO2–SiO2 catalysts with tailored pore architecture and high epoxidation activity. *Chem. Mater.* 2019, *31*, 1610-1619.

43. Huang, Y.; Ho, W.; Ai, Z.; Song, X.; Zhang, L.; Lee, S., Aerosol-assisted flow synthesis of B-doped, Ni-doped and B–Ni-codoped TiO2 solid and hollow microspheres for photocatalytic removal of NO. *Appl. Catal. B* 2009, *89* (3-4), 398-405.

44. Wang, C.; Bai, H., Catalytic Incineration of Acetone on Mesoporous Silica Supported Metal Oxides Prepared by One-Step Aerosol Method. *Ind. Eng. Chem. Res.* 2011, *50* (7), 3842-3848.

45. Debecker, D. P.; Stoyanova, M.; Rodemerck, U.; Colbeau-Justin, F.; Boissère, C.; Chaumonnot, A.; Bonduelle, A.; Sanchez, C., Aerosol route to nanostructured WO3-SiO2-Al2O3 metathesis catalysts: Toward higher propene yield. *Appl. Catal. A* 2014, *470* (0), 458-466.

46. Maksasithorn, S.; Praserthdam, P.; Suriye, K.; Debecker, D. P., Preparation of super-microporous WO3–SiO2 olefin metathesis catalysts by the aerosol-assisted sol–gel process. *Microporous Mesoporous Mater.* 2015, *213* (0), 125-133.

47. Chaumonnot, A.; Tihay, F.; Coupé, A.; Pega, S.; Boissière, C.; Grosso, D.; Sanchez, C., New aluminosilicate materials with hierarchical porosity generated by aerosol process. *Oil Gas Sci. Technol.* 2009, *64* (6), 681-696.

48. Godard, N.; Vivian, A.; Fusaro, L.; Cannavicci, L.; Aprile, C.; Debecker, D. P., High-yield synthesis of ethyl lactate with mesoporous SnSi mixed oxide catalysts prepared by the aerosol-assisted sol-gel process. *ChemCatChem* 2017, *9*, 2211-2218.

49. Sassoye, C.; Muller, G.; Debecker, D. P.; Karelovic, A.; Cassaignon, S.; Pizarro, C.; Ruiz, P.; Sanchez, C., A sustainable aqueous route to highly stable suspensions of monodispersed nano ruthenia. *Green Chem.* 2011, *13* (11), 3230-3237.

50. Debecker, D. P.; Farin, B.; Gaigneaux, E. M.; Sanchez, C.; Sassoye, C., Total oxidation of propane with a nano-RuO2/TiO2 catalyst. *Appl. Catal. A* 2014, *481*, 11-18.

51. Rodriguez-Carvajal, J.; Roisnel, T. WinPLOTR, a graphic tool for powder diffraction, Institut Laue Langevin (2016). www.cdifx.univ-rennes1.fr/winplotr.

52. Glisoni, R. J.; Sosnik, A., Novel Poly(Ethylene Oxide)-b-Poly(Propylene Oxide) Copolymer-Glucose Conjugate by the Microwave-Assisted Ring Opening of a Sugar Lactone. *Macromol. Biosci.* 2014, *14* (11), 1639-1651.

53. Socrates, G., *Infrared and Raman Characteristic Group Frequencies: Tables and Charts, 3rd Edition*. Wiley: 2004; p 366.

54. Musić, S.; Gotić, M.; Ivanda, M.; Popović, S.; Turković, A.; Trojko, R.; Sekulić, A.; Furić, K., Chemical and micro structural properties of TiO2 synthesized by sol-gel procedure. *Mater. Sci. Eng. B* 1997, *47* (1), 33-40.

55. Vasconcelos, D.; Costa, V.; Nunes, E.; Sabioni, A.; Gasparon, M.; Vasconcelos, W., Infrared Spectroscopy of Titania Sol-Gel Coatings on 316L Stainless Steel. *Mater. Sci. Appl.* 2011, *2* (10), 1375-1382.

56. Burgos, M.; Langlet, M., The sol-gel transformation of TIPT coatings: a FTIR study. *Thin Solid Films* 1999, *349* (1), 19-23.

57. Oveisi, H.; Suzuki, N.; Beitollahi, A.; Yamauchi, Y., Aerosol-assisted fabrication of mesoporous titania spheres with crystallized anatase structures and investigation of their photocatalitic properties. *J. Sol-Gel Sci. Technol.* 2010, *56* (2), 212-218.

58. Mason, G., The effect of pore space connectivity on the hysteresis of capillary condensation in adsorption—desorption isotherms. *J. Colloid Interface Sci.* 1982, *88* (1), 36-46.

59. Fernández, C.; Sassoye, C.; Debecker, D. P.; Sanchez, C.; Ruiz, P., Effect of the size and distribution of supported Ru nanoparticles on their activity in ammonia synthesis under mild reaction conditions. *Appl. Catal. A* 2014, *474*, 194-202.

60. Cassaignon, S.; Koelsch, M.; Jolivet, J.-P., Selective synthesis of brookite, anatase and rutile nanoparticles: thermolysis of TiCl4 in aqueous nitric acid. *J. Mater. Sci.* 2007, *42* (16), 6689-6695.

61. Zhang, H.; Banfield, J. F., Phase transformation of nanocrystalline anatase-to-rutile via combined interface and surface nucleation. *J. Mater. Res.* 2011, *15* (2), 437-448.

62. Sönmezoğlu, S.; Çankaya, G.; Serin, N., Phase transformation of nanostructured titanium dioxide thin films grown by sol–gel method. *Appl. Phys. A* 2012, *107* (1), 233-241.

63. You, Y. F.; Xu, C. H.; Xu, S. S.; Cao, S.; Wang, J. P.; Huang, Y. B.; Shi, S. Q., Structural characterization and optical property of TiO2 powders prepared by the sol–gel method. *Ceram. Int.* 2014, *40* (6), 8659-8666.

64. Perego, C.; Wang, Y.-h.; Durupthy, O.; Cassaignon, S.; Revel, R.; Jolivet, J.-P., Nanocrystalline Brookite with Enhanced Stability and Photocatalytic Activity: Influence of Lanthanum(III) Doping. *ACS Appl. Mater. Interfaces* 2012, *4* (2), 752-760.

65. Fröhlich, K.; Ťapajna, M.; Rosová, A.; Dobročka, E.; Hušeková, K.; Aarik, J.; Aidla, A., Growth of High-Dielectric-Constant TiO2 Films in Capacitors with RuO2 Electrodes *Electrochem. Solid-State Lett.* 2008, *11* (6), G19-G21.

66. Wang, X.; Gordon, R. G., High-Quality Epitaxy of Ruthenium Dioxide, RuO2, on Rutile Titanium Dioxide, TiO2, by Pulsed Chemical Vapor Deposition. *Cryst. Growth Des.* 2013, *13* (3), 1316-1321.

67. Komanoya, T.; Kobayashi, H.; Hara, K.; Chun, W.-J.; Fukuoka, A., Catalysis and characterization of carbon-supported ruthenium for cellulose hydrolysis. *Appl. Catal. A* 2011, *407* (1), 188-194.

For Table of Contents Only

